Engineering Science and Technology, an International Journal 41 (2023) 101386

HOSTED BY

Contents lists available at ScienceDirect

Engineering Science and Technology, an International Journal

journal homepage: www.elsevier.com/locate/jestch

Full Length Article

Fluid-thermal characteristics of high-voltage line-start permanent magnet synchronous motor based on bidirectional hydraulic-thermal network coupling

Yongming Xu [a,*], Ziyi Xu [b], Yang Meng [b], Yaodong Wang [c]

[a] School of Electrical and Information Engineering, Changzhou Institute of Technology, Changzhou 213032, China
[b] School of Electrical and Electronic Engineering, Harbin University of Science and Technology, Harbin 150080, China
[c] Department of Engineering, Durham University, Durham DH1 3LE, UK

A R T I C L E I N F O

Article history:
Received 5 October 2022
Revised 8 March 2023
Accepted 9 March 2023
Available online 22 March 2023

Keywords:
High-voltage LSPMSM
Bidirectional hydraulic-thermal network coupling
Axial and radial mixed ventilation cooling
Fluid-thermal characteristics

A B S T R A C T

This paper concerns the fluid-thermal characteristics of a high-voltage line-start permanent magnet synchronous motor (LSPMSM). A bidirectional hydraulic-thermal network coupling methodology is proposed and applied to the fluid-thermal characteristics calculation. The proposed method can fully account for fluid-thermal interactions to achieve an accurate prediction. According to the structural features of the motor with axial and radial mixed ventilation cooling, the global hydraulic network is established by connecting the local indenter elements and hydraulic resistances. The global thermal network is established based on heat source distribution and heat transfer paths. The temperature rise of the motor ranges from 45.8 K to 84.9 K. The hotspot appears at the lower end-winding on the drive side, and the lowest temperature rise occurs on the nondrive side of the shaft. Moreover, the experimental platform is built to verify the accuracy of the proposed method, and the relative error is 2.2% and 2.9%.

1. Introduction

High-voltage line-start permanent magnet synchronous motors (LSPMSM) are ideal drive motors for fan and pump loads due to their superiority in efficiency, compactness, and convenience of starting [1]. The continuous development of these application scenarios has brought about increased requirements for LSPMSM in terms of speed, torque, and power. These requirements can be achieved by raising the electromagnetic load of the motor. However, the losses generated in the motor also increase with the electromagnetic load, resulting in a high temperature rise inside the motor. Excessive temperature rise will weaken the electromagnetic performance and operational reliability of LSPMSM [2]. Therefore, accurately predicting the fluid-thermal characteristics is essential for a reliable motor design [3].

There are two mainstream methods for calculating motor fluid-thermal characteristics: computational fluid mechanics (CFD) and lumped parameter thermal network (LPTN). CFD can achieve accurate and detailed fluid-thermal characteristics for the motor. However, it is much more demanding in terms of modeling and calculation costs [4]. In contrast, the application of LPTN enables a quick fluid-thermal characteristics calculation [5]. By increasing the number of nodes and thermal resistance of LPTN and improving the determination of crucial LPTN parameters, LPTN can also achieve fluid-thermal characteristics calculation with high accuracy and detail. Therefore, more and more scholars are applying LPTN for thermal analysis of the motor.

To date, many researches about the fluid-thermal characteristics calculation have been performed based on LPTN [6–8]. The convective heat transfer coefficients (CHTC) in existing research are calculated mainly by empirical formulas [9,10]. It means that the geometrical features of structures inside the motor, such as the stator end winding, are not sufficiently considered when calculating the CHTC. In addition, the cooling fluid is usually simplified as a node, and it is assumed that its temperature is constant [11,12]. All the above treatments are not conducive to the improvement of LPTN accuracy.

Many investigations have been conducted to provide a guideline for improving the accuracy of LPTN. It has been proven that the calculated temperature distribution is closer to the actual situation when more nodes are established in the axial direction for the cooling fluid [13]. It is also applicable to other structures, such as windings [14]. Some literature has also discussed determining CHTC for LPTN through new methods, such as the stepwise quadratic specification method [15] and the hydraulic network method

* Corresponding author.
E-mail address: xuyongming@czu.edu.cn (Y. Xu).

https://doi.org/10.1016/j.jestch.2023.101386
2215-0986/

[16,17]. Moreover, more and more studies apply CFD to calculate CHTC, especially for the fluid–solid interface with complex shapes or intense heat exchange, such as the end-winding [18,19], air gap [20,21] and hollow shaft [22]. However, applying CFD to calculate CHTC is time-consuming.

In summary, although many studies have used LPTN to predict motor temperature distributions, few studies have considered the interaction between temperature and fluid fields when applying LPTN for temperature prediction, or have not adequately considered. Thus, the thermophysical properties of the air applied in the calculations deviate from the actual situation. It is difficult to accurately predict the thermal behavior within the motor. In view of the above, this paper proposes a method for calculating fluid-thermal characteristics based on bidirectional hydraulic-thermal network coupling. In terms of model building, the fluid nodes of the thermal network model correspond to the branches of the hydraulic network model. During the calculation, the model parameters of the hydraulic and thermal networks are updated through the same fluid nodes and branches in a continuous iterative process, which can take into account the interaction between the fluid and temperature fields and the changes in the thermophysical parameters of the air. The bidirectional coupling analysis between the two models is realized. This method enables fast and accurate prediction of the fluid-thermal characteristics of the high-voltage LSPMSM. Furthermore, the interaction between the fluid and temperature fields is fully considered in the calculation process.

The remainder of this paper is organized as follows. Firstly, the methodology of this research is introduced, including the electromagnetic parameters and cooling arrangement of the prototype, the construction of the hydraulic network and thermal network, the coupling method between the two networks, and experimental platform. Then, the fluid-thermal characteristics of the motor are analyzed and discussed in detail and depth. Finally, compare the calculated results with the experimental values to verify the accuracy of the calculated results.

2. Methodology

2.1. Description of the high-voltage LSPMSM

The prototype is an air-air cooled high-voltage LSPMSM with axial and radial mixed ventilation. The cooling air flow path is shown in Fig. 1(a). It can be seen that the path is divided into two parts: the internal air path and the external air path. The internal air path includes seven radial ventilation ducts and one centrifugal fan at each side end. The external air path comprises abundant cooling pipes and a centrifugal fan at the inlet of the external air path.

Inside the motor, the main flow path of cooling air can be divided into three parts. One passes through both the radial ventilation ducts of the stator and rotor (marked a in Fig. 1(a)). Another one passes through the air gap and the radial ventilation ducts of the stator (marked b in Fig. 1(a)). The rest cools the end-winding under the action of the centrifugal fan (marked c in Fig. 1(a)). For the external air path, the centrifugal fan at the inlet draws cold external air into the cooler. After that, the air will take away the heat generated in the motor through the heat exchange between the cooling pipe wall and the air in the internal air path.

The schematic diagram of the prototype structure is shown in Fig. 1(b). Seven radial ventilation ducts divide the stator and rotor core into eight sections. From the drive side to the nondrive side, the core sections are numbered sequentially from 1 to 8, and the radial ventilation ducts are numbered from 1 to 7. The basic dimensions and performance parameters of the LSPMSM are listed in Table 1.

2.2. Hydraulic network model

The following assumptions are made when constructing the hydraulic network:

(1) Since the flow velocity of air is much smaller than the speed of sound, less than Mach 0.3. So, air is considered as incompressible fluid.
(2) Because complex three-dimensional flow phenomena, such as vortices, are ignored, the flow studied is considered to be one-dimensional pipe flow. Therefore, the flow rate obtained is the average value over the cross-section of the ventilation channels in the flow path.
(3) The effect of stator and rotor slotting is ignored to simplify the stator and rotor core geometries. Simplify the inner surface of the stator and the outer surface of the rotor as cylindrical surfaces to facilitate the fluid network modeling.

The hydraulic network model is established based on the continuity and Bernoulli equations. The pressure balance equation in each circuit of the hydraulic network model is [23]:

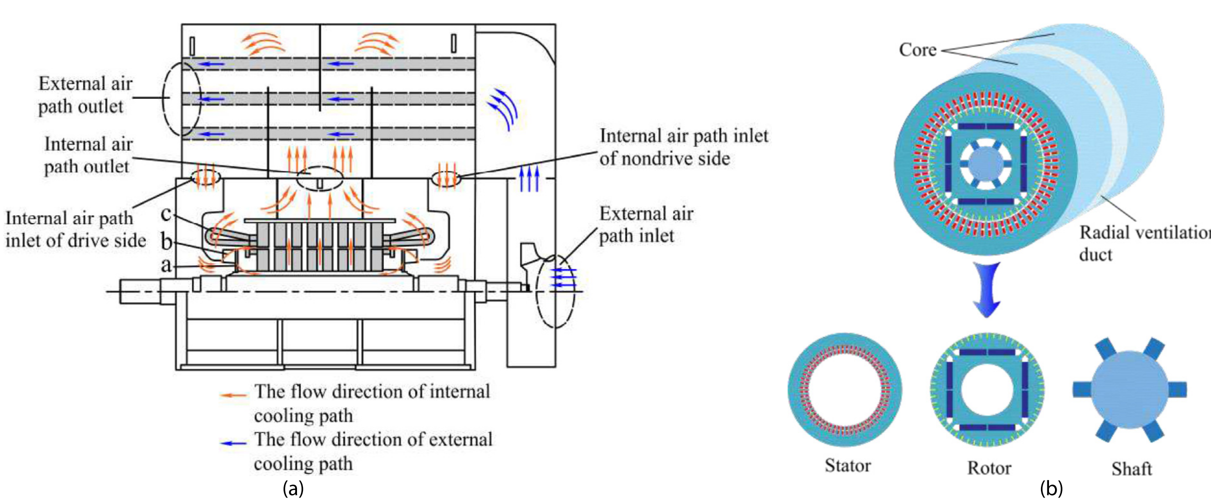

Fig. 1. Prototype cooling arrangement and structure. (a) Cooling air flow path. (b) Prototype structure.

Table 1
The basic dimensions and performance parameters of the LSPMSM.

Parameters	Value	Parameters	Value
Rated power (kW)	280	Rated voltage (kV)	10
Rated Frequency (Hz)	50	Rated speed (rpm)	1500
Power factor	0.957	Efficiency (%)	96
Core length (mm)	380	Air gap thickness (mm)	2.5
Stator outer diameter (mm)	670	Stator inner diameter (mm)	423
Width of radial ventilation ducts (mm)	10	Number of radial ventilation ducts	7
Stator/Rotor slots number	60/52	Insulation degree	H
Permanent magnet material	N38UH	Cage material	H62 brass

$$\sum_{j=1}^{m} p_{i,j} = \sum_{k=1}^{n} Z_{i,k} Q_{i,k}^{2} \tag{1}$$

where $p_{i,j}$ is the pressure generated by the indenter element j in circuit i, $Z_{i,k}$ is the hydraulic resistance of the branch k in circuit i, and $Q_{i,j}$ is the flow of the air of the branch k in circuit i.

Each circuit of the hydraulic network model has an indenter element to offset the pressure drop loss, including frictional pressure drop loss and local pressure drop loss. The indenter elements of the motor include the centrifugal fan and rotor radial ventilation duct steel. Due to the nonlinearity of hydraulic resistance, the operating point of indenter elements is determined according to the *p*-*Q* characteristic curves, as shown in Fig. 2(a). The relationship between the indenter and the ratio of no-load static pressure and maximum flow of short circuit is expressed by equation (2):

$$p = p_0\left[1 - (Q/Q_m)^2\right] \tag{2}$$

where p_0 is the no-load static pressure, and Q_m is the maximum short-circuit flow.

The frictional and local pressure drop losses can be equivalent to the hydraulic resistance. The calculation formula for hydraulic resistance is given by (3):

$$Z_{i,k} = \zeta \frac{\rho}{2A^2} \tag{3}$$

where ζ is the resistance coefficient, ρ is the fluid density, and A is the cross-sectional area.

According to the cause of pressure loss, hydraulic resistance can be divided into friction pressure drop hydraulic resistance and local pressure drop hydraulic resistance. The resistance coefficients of the two hydraulic resistances are determined in different ways. The frictional resistance coefficient is related to the flow regime of the air and the roughness of the pipeline. The former is determined by the *Reynolds* number:

$$Re = \frac{\nu d_e}{\upsilon} \tag{4}$$

where ν is the cooling air flow rate, d_e is the equivalent diameter of the branch ventilation duct, υ is the kinematic viscosity of air. The air in the motor is in a turbulent state, and the calculation formula of the frictional resistance coefficient is:

$$\zeta = 1.42\left[\lg(Re \cdot (d_e/\varepsilon))\right]^{-2} \tag{5}$$

where ε is the roughness of the ventilation duct.

Unlike the frictional resistance coefficient, the local resistance coefficient is related to the flow regime and the change in pipe shape. The common local resistance coefficients of the motor are caused by sudden expansion, sudden reduction, and pipe bending, as shown in Fig. 2(b). Formulas (6)-(7) explain the relationship

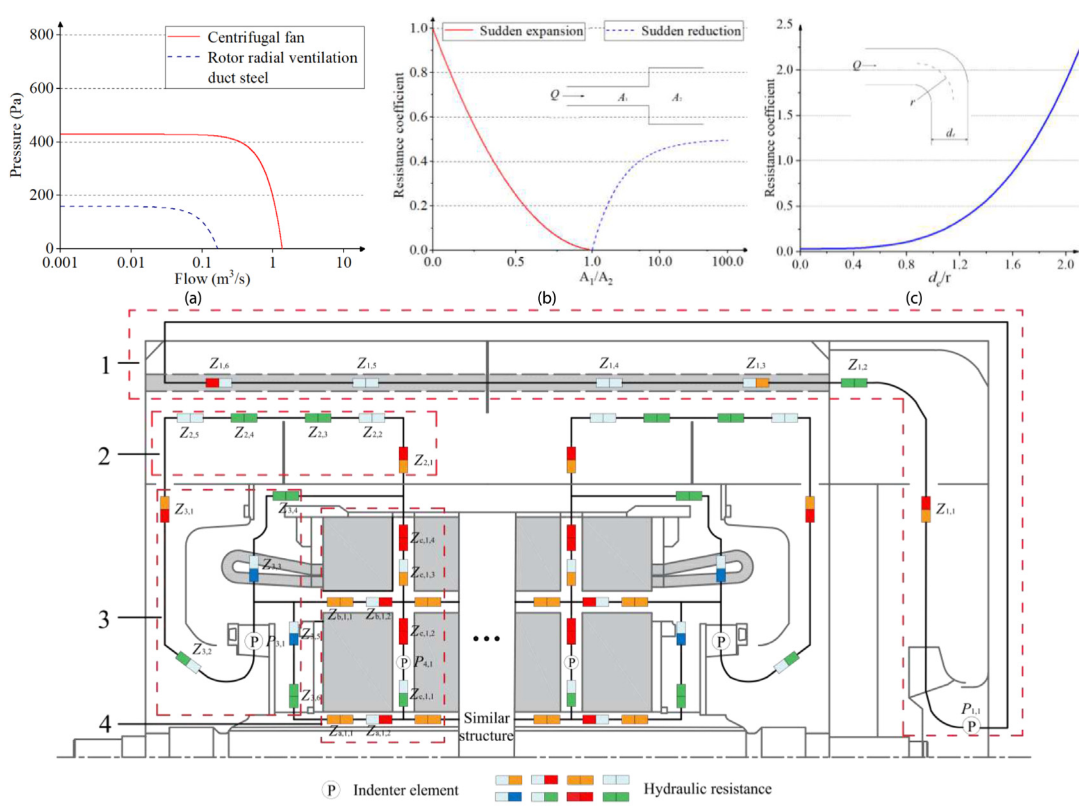

Fig. 2. Hydraulic network construction and model. (a) Indenter element *p*-*Q* characteristic curves. (b) Variation of local resistance coefficient with section area ratio. (c) Variation of local resistance coefficient with d_e/r. (d) Hydraulic network model.

between the local resistance coefficient and the area change rate. When A_2 is infinite, the outlet resistance coefficient can be obtained as 1, and when A_1 is infinite, the inlet resistance coefficient can be obtained as 0.5.

$$\zeta = [1 - (A_1/A_2)]^2 \tag{6}$$

$$\zeta = 0.5(1 - A_2/A_1) \tag{7}$$

Formula (8) explains the relationship between the local resistance coefficient and pipe curvature. The common local resistance coefficient of the motor is caused by right-angle bending, as shown in Fig. 2(c).

$$\zeta = (0.031 + 0.163(d_e/r)^{3.5}) \cdot (\theta/90) \tag{8}$$

where d_e is the diameter of the ventilation duct, r is the curvature diameter of ventilation duct, and θ is the corner of the ventilation duct.

Since the internal and external air paths are not connected, their hydraulic network models are independent. According to the internal and external air paths displayed in Fig. 1(a), the local hydraulic network model is constructed by connecting the indenter element in each region with the hydraulic resistance. Then, each local hydraulic network model is connected to form the global hydraulic network model.

The global hydraulic network model of the motor is shown in Fig. 2(d). Zones 1–4 represent the external air path, the internal air path in the cooler, the internal air path in the end region, and the internal air path in the active region of the motor, respectively. The component subscript for zones 1–3 consists of two parts. The former represents the zone number, and the latter represents the serial number of the component. For the component in zone 4, the subscript consists of three parts. The first represents the position, where subscript a is the axial ventilation ducts, subscript b is the air gap, and subscript c is the radial ventilation ducts. The second represents the number of axial locations. The subscripts of the air gap and axial ventilation ducts of the rotor range from 1 to 8, and the subscripts of the radial ventilation ducts of the rotor and stator range from 1 to 7. The last is the same as zones 1–3 and represents the serial number of the component. In addition, the hydraulic resistance caused by different reasons is distinguished by colors. Orange represents inlet hydraulic resistances, red represents outlet hydraulic resistances, green represents bending hydraulic resistances, blue represents hydraulic resistances across the cylinder, and gray represents frictional hydraulic resistances.

Take zone 1 as an example. Outside air enters zone 1 by the action of the centrifugal fan ($P_{1,1}$). Since the area suddenly becomes smaller and then suddenly becomes larger, it generates inlet pressure drop loss and outlet pressure drop loss, which are equivalent to hydraulic resistance $Z_{1,1}$. Then, under the action of the air guide plate, the flow direction of air changes, resulting in bending pressure drop loss $Z_{1,2}$. The zone of cooling pipes is divided into four parts according to the number of the baffle plates. The inlet pressure drop occurs when air enters the cooling pipe $Z_{1,3}$, and the outlet pressure drop occurs when the cooling air leaves the cooling pipe $Z_{1,6}$. $Z_{1,4}$ and $Z_{1,5}$ represent the frictional loss along with the flow in the cooling pipe. Eventually, air returns to the outside, so the hydraulic network of the external cooling path forms a closed loop. Other zones are similar and will not be repeated.

2.3. Thermal network model

The following assumptions are made when constructing the thermal network:

(1) The magnitude of the radial and axial thermal resistance does not vary with the heat flow distribution, but only affected by the average temperature in the region.
(2) Radiant heat transfer is not considered. Only heat conduction between solid parts and convective heat transfer at the fluid–solid interface are considered.
(3) Each contact surface is in good contact. The influence of contact thermal resistance is ignored.
(4) The losses generated in the motor are evenly distributed and are all dissipated to the outside through the cooler.

According to the law of thermodynamics and energy conservation, all nodes of the thermal network model satisfy the equation:

$$q_i = \sum_{j=1}^{n} \frac{T_{i,j} - T_{i,0}}{R_{i,j}} + \Phi_i \tag{9}$$

where q_i is the heat flowing out of the node i, $T_{i,j}$ is the temperature of the node adjacent to node i, $T_{i,0}$ is the temperature of the node i, $R_{i,j}$ is the thermal resistance between the node i and the adjacent node, and Φ_i is the heat source of the node i.

Nodes in the thermal network model can be divided into active nodes and passive nodes. The active nodes are also divided into two types. One is the solid node in the loss-generating region, whose heat source is the equivalent heat flow source of the sum of losses in the region. The other one is the fluid node that absorbs heat, whose heat source is the heat pressure source that takes the influence of heat absorption on the adjacent fluid node into account. The heat pressure source can be calculated using the following formula:

$$\Delta T = \frac{\sum P}{c_v Q} \tag{9}$$

where ΔT is the temperature change of air, $\sum P$ is the heat absorbed by air, c_v is the specific heat capacity of air, and Q is the flow of air.

The heat transfer mode in the motor is mainly conduction and convection heat transfer. Heat conduction occurs between solid components, and convective heat transfer appears at the fluid–solid interface. The corresponding thermal resistance calculation formula is:

$$R_{i,j} = \begin{cases} l/\lambda_s S \\ 1/\alpha S \end{cases} \tag{10}$$

where l is the effective length of the heat transfer path, S is the effective area of the heat transfer path, λ_s is the thermal conductivity of the solid, and α is the convective heat transfer coefficient.

$$\alpha = \frac{\lambda_{air}}{L} Nu \tag{11}$$

where λ_{air} is the thermal conductivity of air, L is the characteristic size, and Nu is the *Nusselt* number.

The equation for the *Nusselt* number is as follows [24]:

$$Nu = 0.023 Re^{0.8} Pr^{0.4} \tag{12}$$

where Pr is the *Prandtl* number.

For the airflow in the air gap, the axial velocity component of the air in the air gap can be obtained through the hydraulic network model. The rotational motion of the rotor makes the air in the air gap have circumferential velocity component. The magnitude of the circumferential velocity component is related to the rotor speed. The air velocity in the air gap can be obtained by combining the axial velocity component and the circumferential velocity component. On this basis, the convective heat transfer coefficient of each surface in the air gap can be calculated, and the value of convective thermal resistance can be determined.

The basic geometric shapes used in motors include hollow cylinders and flat plates. The equivalent thermal model of the hollow cylinder is shown in Fig. 3(a), and the thermal resistance calculation formulas are as follows:

$$\begin{cases} R_{a1} = R_{a2} = \frac{2}{\pi}\frac{l}{\lambda_a(r_2^2-r_1^2)} \\ R_{r1} = \frac{1}{2\pi\lambda_r l}\ln\frac{r_2+r_1}{2r_1} \\ R_{r2} = \frac{1}{2\pi\lambda_r l}\ln\frac{2r_2}{r_2+r_1} \end{cases} \tag{13}$$

where R_{a1}, R_{a2} are the thermal resistances of axial heat conduction, λ_a is the axial thermal conductivity of materials, R_{r1}, R_{r2} are the thermal resistances of radial heat conduction, and λ_r is the radial thermal conductivity of materials.

The equivalent thermal model of the flat plate structure is shown in Fig. 3(b), and the calculation formulas of thermal resistance are as follows:

$$\begin{cases} R_{a1} = R_{a2} = \frac{l}{2\lambda_a hw} \\ R_{c1} = R_{c2} = \frac{w}{2\lambda_c hl} \\ R_{r1} = R_{r2} = \frac{h}{2\lambda_r wl} \end{cases} \tag{14}$$

where R_{c1}, R_{c2} are the thermal resistances of circumferential heat conduction, λ_c is the circumferential thermal conductivity of materials.

A complete representation of the individual conductors and surrounding insulation material would add significant complexity to the thermal network model. Therefore, based on the principle of constant cross-sectional area, the multiple conductors are simplified to a single conductor, and the multi-layer insulation is simplified to a single layer, as shown in Fig. 3(c). Moreover, the equivalent thermal conductivity is calculated [25].

Due to the radial asymmetry of the permanent magnet (PM) arrangement, it is much more complex to model the PM and rotor core yoke. To simplify the thermal network model, it is necessary to make an equivalent operation for PM. The premise of equivalence is that the radial heat transfer coefficients of the PM and the rotor core are close, and the heat source is not considered in PM and the rotor core yoke. On this basis, PM with the rectangular cross-section is equivalent to the circular cross-section according to the principle that the center of PM is fixed and the area and thickness of PM are constant. The rotor structure before and after equivalence is shown in Fig. 3(d). Because of the small width of the magnetic bridge, the heat transfer between the outer yoke and the inner yoke of the rotor core is ignored. The physical properties of the materials involved are listed in Table 2.

In order to realize the coupling calculation with the hydraulic network, the fluid nodes of the thermal network model should correspond to the branches of the hydraulic network. Therefore, the fluid nodes of the thermal network model correspond to the branches of the internal and external hydraulic network models constructed in Section 2.2.

According to the heat transfer path and loss distribution, the local thermal network models of each solid region are constructed. Then, the local thermal network models of each solid region are connected through the fluid nodes to form the global thermal network model according to the flow paths of the internal and external air paths.

The global thermal network model of the motor is shown in Fig. 4. The thermal network model is divided into the end winding region, core region, and radial ventilation duct region along the axial direction. Each region is composed of many different structures in the radial direction. Therefore, the label of each node consists of two parts. The first represents the axial position, where labels 0 and 9 are the end winding region, 1–8 are the core region, 10 is the cooler region, and 11–17 are the radial ventilation duct region. The latter represents different structures in the radial direction.

Table 2
Material physical properties.

Material	Density (kg/m^3)	Specific heat capacity (J/(kg·K))	Thermal conductivity (W/(m·K))
N38UH	7400	450	44.2
Equivalent insulation	1800	1000	0.18
Silicon steel sheet	7650	381	42.5/42.5/4.5 (radial/circumferential/axial)
H62 brass	8978	381	387.6

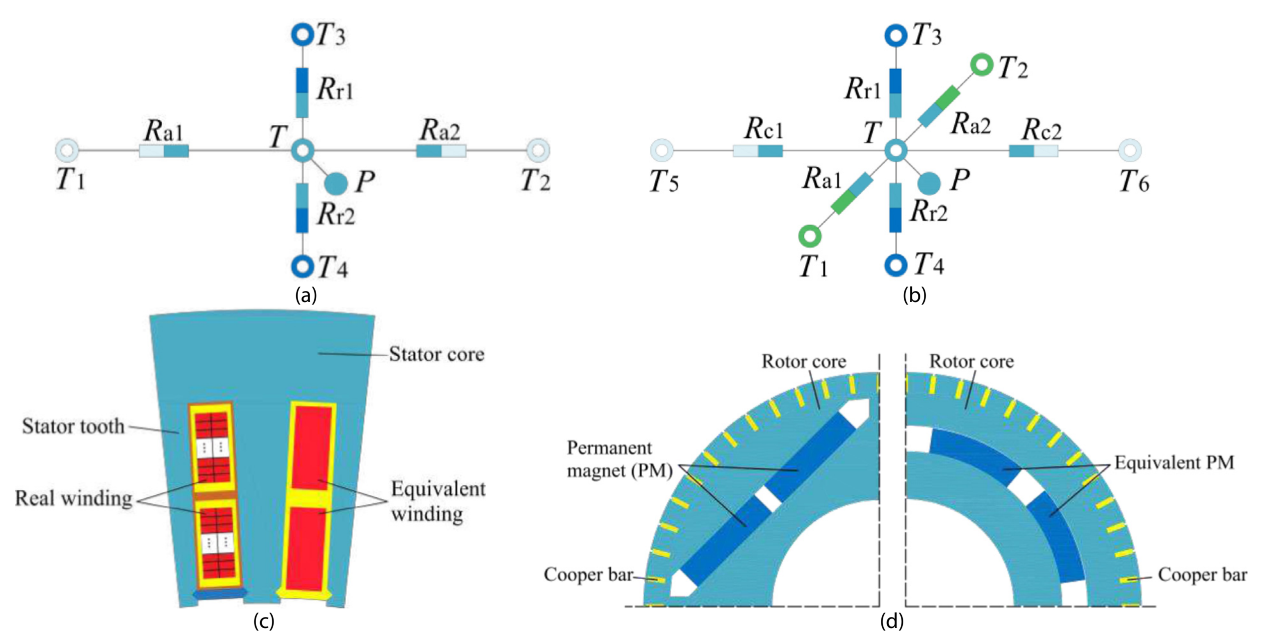

Fig. 3. Thermal network construction. (a) Equivalent thermal model of hollow cylinder. (b) Prototype structure. (c) Winding equivalence. (d) PM equivalence.

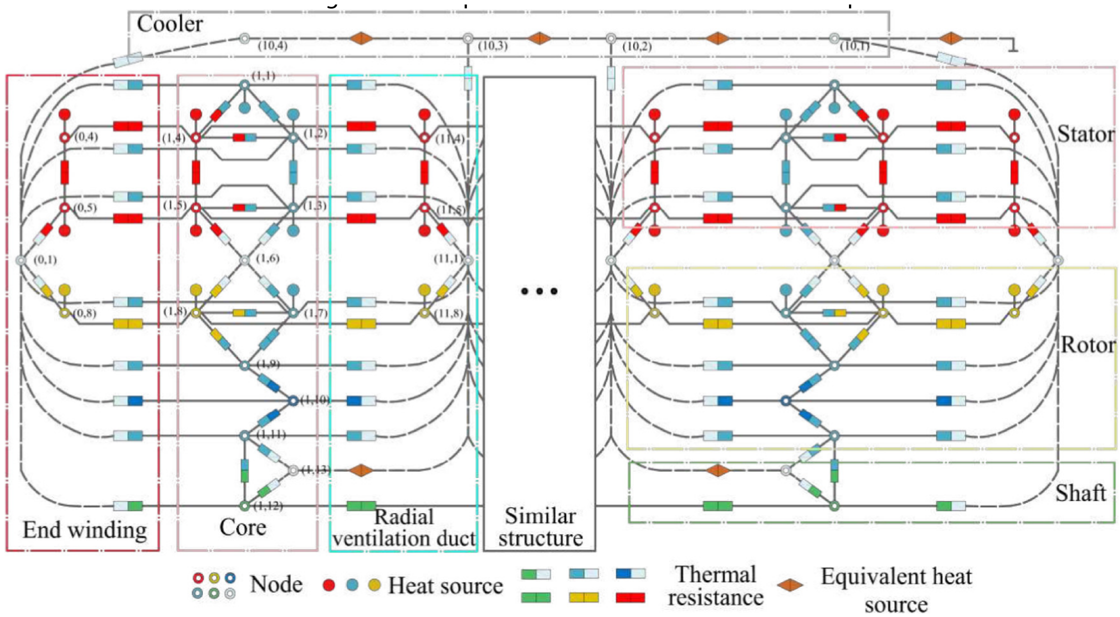

Fig. 4. Global thermal network model.

In order to better distinguish different regional nodes, regional nodes and thermal resistances are distinguished by color. The red represents the stator winding, the light blue represents the iron core, the yellow represents the rotor copper bar, the dark blue represents the PM, the green represents the shaft, and the gray represents the air.

Take the No. 1 core region as an example. The stator region includes the stator yoke node (1,1), stator tooth nodes (1,2) and (1,3), and stator winding nodes (1,4) and (1,5). All of them are nodes with heat sources. The stator yoke node is connected to the air gap node (1,6) through the stator teeth and the stator winding. In addition, circumferential heat transfer between the stator winding and the stator teeth at the same radial position is also considered ((1,2) and (1,4), (1,3) and (1,5)). The stator region is connected to the rotor region through the air gap node (1,6), and heat is transferred to the rotor region through the rotor tooth node (1,7) and the rotor copper bar node (1,8), respectively. The rotor teeth and the rotor copper bar each have a heat source, and there is circumferential heat transfer between them. Then, heat is transferred to the inner yoke node (1,11) through the outer yoke node (1,9) and PM node (1,10). Finally, a portion of the heat directly enters the rotor axial ventilation duct node (1,13), and another portion indirectly enters the rotor axial ventilation duct node through the shaft node (1,12). Other regions are similar and will not be repeated.

2.4. Bidirectional hydraulic-thermal network coupling method

According to the above description, the parameters of the hydraulic and thermal network components are associated with each other. The change in one network parameter affects not only itself but also the others. Therefore, bidirectional coupling calculation is essential for calculating the fluid-thermal characteristics of the motor more accurately.

For the hydraulic network, the hydraulic resistance of each branch is related to the temperature of the air. As the temperature increases, the kinematic viscosity of the air increases, which leads to an increase in the hydraulic resistance of the branch pipes and, ultimately, a decrease in the flow rate. And vice versa.

For the thermal network, the reduction in air flow will weaken the convective heat transfer intensity, which will increase the corresponding convection thermal resistance. Ultimately, the amount of heat emitted from the ventilation ducts will decrease. The flow chart for the bidirectional hydraulic-thermal network coupling calculation is shown in Fig. 5.

Firstly, assuming the initial air temperature in each zone, the hydraulic network can be solved to obtain the air flow in each branch. Secondly, the convective heat transfer coefficient of each fluid–solid interface is calculated based on the hydraulic network results, and the thermal network will be solved. Then, the temperature of each node and the heat flux of each branch are obtained.

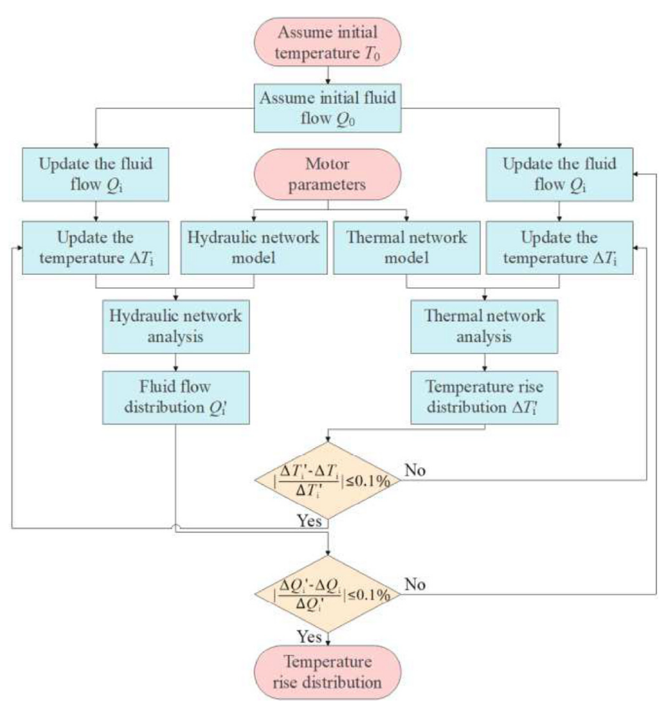

Fig. 5. The flow chart of bidirectional hydraulic-thermal network coupling calculation.

Table 3
Losses in the motor.

Item	Value (W)
Stator core teeth iron loss	1940
Stator core yoke iron loss	1694.4
Rotor core teeth iron loss	155.2
Stator winding copper loss	1805.2

The heat pressure source will be updated until its value meets the residual. After that, the physical properties of air are recalculated to update the hydraulic network parameters. The global motor temperature rise can be obtained through continuous iterative calculations between the hydraulic and thermal networks.

2.5. Heat source calculation

Various losses in the motor are used as the heat source for conducting the temperature rise prediction. It is essential for an accurate prediction. In this paper, 2-D transient electromagnetic analysis is applied to determine the losses, and the analysis is performed by ANSYS Electronics Desktop 2020 R2. The electromagnetic characteristics of the motor can be obtained by 2D transient electromagnetic analysis, such as the amplitude and distribution of the magnetic density, the current amplitude and so on. Then, the various losses in the motor can be calculated according to the formulas (15) and (16), and the results are listed in Table 3. In addition, the losses are also assigned according to 2D transient electromagnetic analysis, and the distribution of losses is listed in Table 4.

$$\begin{aligned} p_{\mathrm{Fe}} &= p_{\mathrm{h}} + p_{\mathrm{c}} + p_{\mathrm{e}} \\ &= k_{\mathrm{h}} f B_{\mathrm{m}}^{\alpha} + k_{\mathrm{c}} f^2 B_{\mathrm{m}}^2 + k_{\mathrm{e}} f^{1.5} B_{\mathrm{m}}^{1.5} \end{aligned} \tag{15}$$

where p_{Fe} is the core loss, p_{h} is the hysteresis loss; p_{c} is the eddy current loss, p_{e} is the additional loss, k_{h} and α are the hysteresis loss coefficients, k_{c} is the eddy current loss coefficient, k_{e} is the additional loss coefficient, f is the frequency of change of the magnetic field and B_{m} is the magnitude of the magnetic flux density.

$$\begin{cases} P_{\mathrm{Cu,\,DC}} = mI^2R \\ P_{\mathrm{Cu,\,AC}} = K_{\mathrm{F}} mI^2R \end{cases} \tag{16}$$

where $P_{\mathrm{Cu,DC}}$ is the direct current copper loss of the motor, $P_{\mathrm{Cu,AC}}$ is the alternating current copper loss of the motor, K_{F} is the alternating current resistance coefficient, m is the number of phases of the motor, I is the effective value of the winding phase current and R is the effective resistance value of the single phase of the stator winding.

The losses are also assigned according to 2D transient electromagnetic analysis. Stator and rotor core losses are uniformly distributed along the axial direction. For the radial direction, although the magnetic flux density of the stator core yoke is lower than that of the stator teeth, the volume is larger. Thus, more core losses are generated in it. In the stator core teeth, the closer to the air gap, the higher the magnitude of the magnetic flux density, and the more core loss is generated. For the rotor core, the core loss generated internally is mainly concentrated in the rotor core teeth. Regarding the stator winding copper loss, its distribution is determined according to the length ratio. The length ratio between the core section and the radial ventilation duct is 4.75:1. In addition, since the length of the stator winding end is much longer than the core section and the radial ventilation duct section, the copper loss is particularly high. The distribution of losses is listed in Table 4.

2.6. Experimental platform

In order to verify the effectiveness of the proposed method and the accuracy of the calculation results, the experimental platform was built. The experimental platform is shown in Fig. 6. The platform includes the prototype, cooler, load motor, and various measuring instruments (Yokogawa WT3000 produced by the Yokogawa testing and measurement company). The rated load test was conducted to measure the temperature rise of the prototype.

Before the temperature rise test, six PT100 thermocouples were pre-embedded on the nondrive side of the stator winding and were evenly distributed in the circumferential direction. The prototype

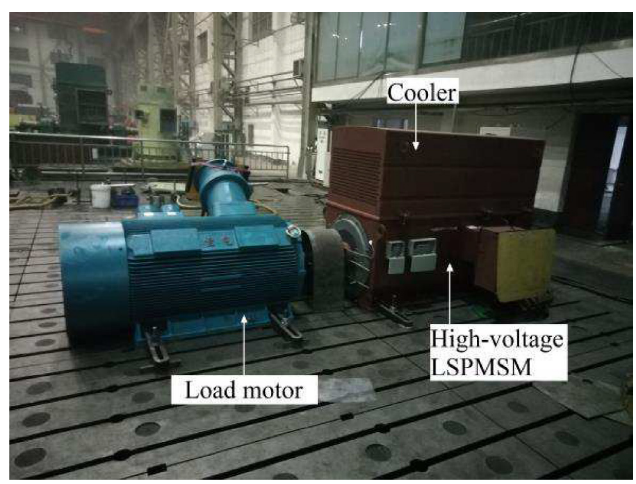

Fig. 6. Experimental platform.

Table 4
Losses distribution.

Region											
Stator core yoke	Node number		(1,1)	(2,1)	(3,1)	(4,1)	(5,1)	(6,1)	(7,1)	(8,1)	
	Loss value (W)		211.8	211.8	211.8	211.8	211.8	211.8	211.8	211.8	
Stator core teeth	Node number		(1,2)	(2,2)	(3,2)	(4,2)	(5,2)	(6,2)	(7,2)	(8,2)	
	Loss value (W)		118.0	118.0	118.0	118.0	118.0	118.0	118.0	118.0	
	Node number		(1,3)	(2,3)	(3,3)	(4,3)	(5,3)	(6,3)	(7,3)	(8,3)	
	Loss value (W)		124.5	124.5	124.5	124.5	124.5	124.5	124.5	124.5	
Stator winding	Node number	(0,4)	(1,4)	(2,4)	(3,4)	(4,4)	(5,4)	(6,4)	(7,4)	(8,4)	(9,4)
	Node number	(0,5)	(1,5)	(2,5)	(3,5)	(4,5)	(5,5)	(6,5)	(7,5)	(8,5)	(9,5)
	Loss value (W)	470.2	89.3	89.3	89.3	89.3	89.3	89.3	89.3	89.3	470.2
	Node number		(11,4)	(12,4)	(13,4)	(14,4)	(15,4)	(16,4)	(17,4)		
	Node number		(11,5)	(12,5)	(13,5)	(14,5)	(15,5)	(16,5)	(17,5)		
	Loss value (W)		18.8	18.8	18.8	18.8	18.8	18.8	18.8		
Rotor core teeth	Node number		(1,7)	(2,7)	(3,7)	(4,7)	(5,7)	(6,7)	(7,7)	(8,7)	
	Loss value (W)		19.4	19.4	19.4	19.4	19.4	19.4	19.4	19.4	

is used as the prime mover, and the load motor is used as the load. The input power of the prototype is read by the power measuring instrument, the output power is obtained by the rotation speed and the torque measuring instrument. The test method strictly follows GB/T 22669-2008. The ambient temperature at the time of the experiment was 298 K. When the temperature change of the motor in 30 min is less than 0.5 K, it is considered that the motor has reached its steady state. Record the data from the temperature sensor at this time. The average of the six sensors data is used as the experimental data to compare with the simulation result.

3. Results and discuss

3.1. Global hydraulic network results

Global hydraulic network results for unidirectional and bidirectional coupling analyses are shown in Fig. 7(a) and (b). It can be

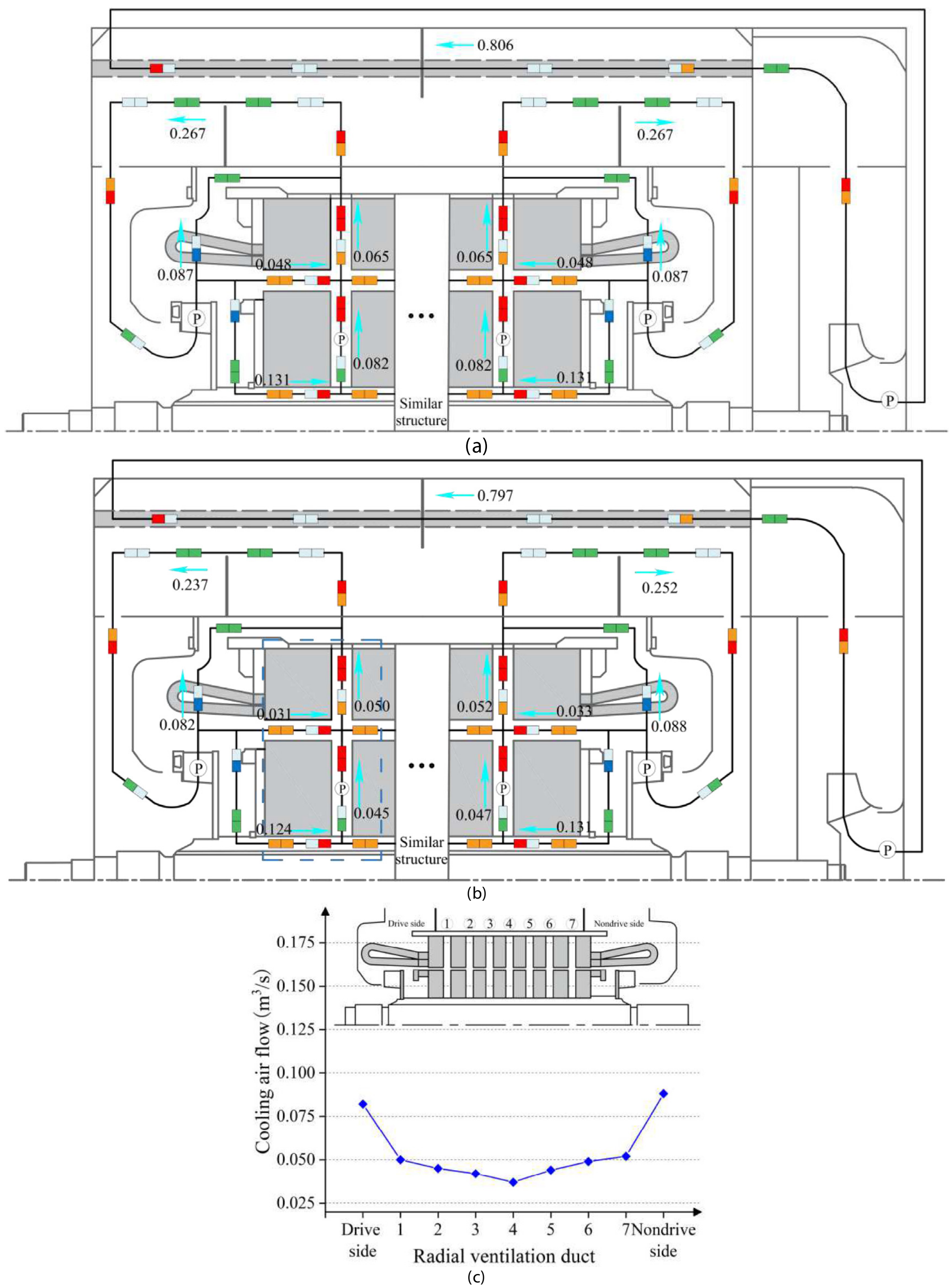

Fig. 7. Hydraulic characteristics results. (a) Global hydraulic network results for unidirectional coupling analysis (m^3/s). (b) Global hydraulic network results for bidirectional coupling analysis (m^3/s). (c) Air flow distribution along axial direction.

seen that the air flow of branches for bidirectional coupling analysis is smaller than that of unidirectional coupling analysis. The total flow of the external and internal air paths in the bidirectional coupling analysis is 0.797 m^3/s and 0.489 m^3/s, respectively, which is 1.12% and 8.43% lower than the unidirectional coupling analysis. In addition, it can be found that the air flow distribution of the bidirectional coupling analysis along the axial is different from the unidirectional one. It is not axisymmetric.

As shown in Fig. 7(b), 34.8% of air returns directly to the cooler via the end space (c in Fig. 1(a)), while the remainder enters the active region of the motor (a and b in Fig. 1(a)). Taking the No. 4 radial ventilation duct as the center, the motor is divided into the drive side and nondrive side regions. The flow in the drive side region is 0.237 m^3/s, which is 6.3% lower than the non-drive side region. It is because the nondrive side air first exchanges heat with the cold air in the external air path, so the nondrive side air temperature is lower than the drive side. The air viscosity of the former is lower than that of the latter. The hydraulic resistance in the corresponding zone also satisfies this relationship.

The air flow distribution of bidirectional coupling analysis along the axial direction is shown in Fig. 7(c). The air flow shows a distribution of high at both ends and low in the middle along the axial direction. The highest flow is in the nondrive side region (0.088 m^3/s), which is 69.2% higher than the maximum flow of the radial ventilation duct (0.052 m^3/s at No. 7 ventilation duct). The lowest flow is No. 4 ventilation duct 0.037 m^3/s. The centrifugal fan located at the end region can provide a greater pressure indenter than the rotor radial ventilation slot steel. Therefore, the further away from the fan, the greater the pressure drop loss of air, then the greater equivalent hydraulic resistance.

3.2. Global thermal network results

The global thermal network results for unidirectional and bidirectional coupling analyses are shown in Fig. 8. Moreover, the global temperature rise distributions of the LSPMSM for unidirectional and bidirectional coupling analyses are listed in Tables 5 and 6. By comparison, it can be found that the overall temperature rise result of the bidirectional coupling analysis is higher than that of the unidirectional coupling analysis. The hotspot temperature rise for bidirectional coupling analysis is 84.9 K, which is 2.7 K higher than unidirectional coupling analysis.

As can be seen from Fig. 8(b), the temperature rises of the motor range from 45.8 K to 84.9 K. The hotspot appears at the lower end-winding on the drive side, and the lowest temperature rise occurs at the non-drive side of the shaft. Furthermore, the temperature rise in the drive side region is slightly higher than that in the non-drive side region. According to the hydraulic network results,

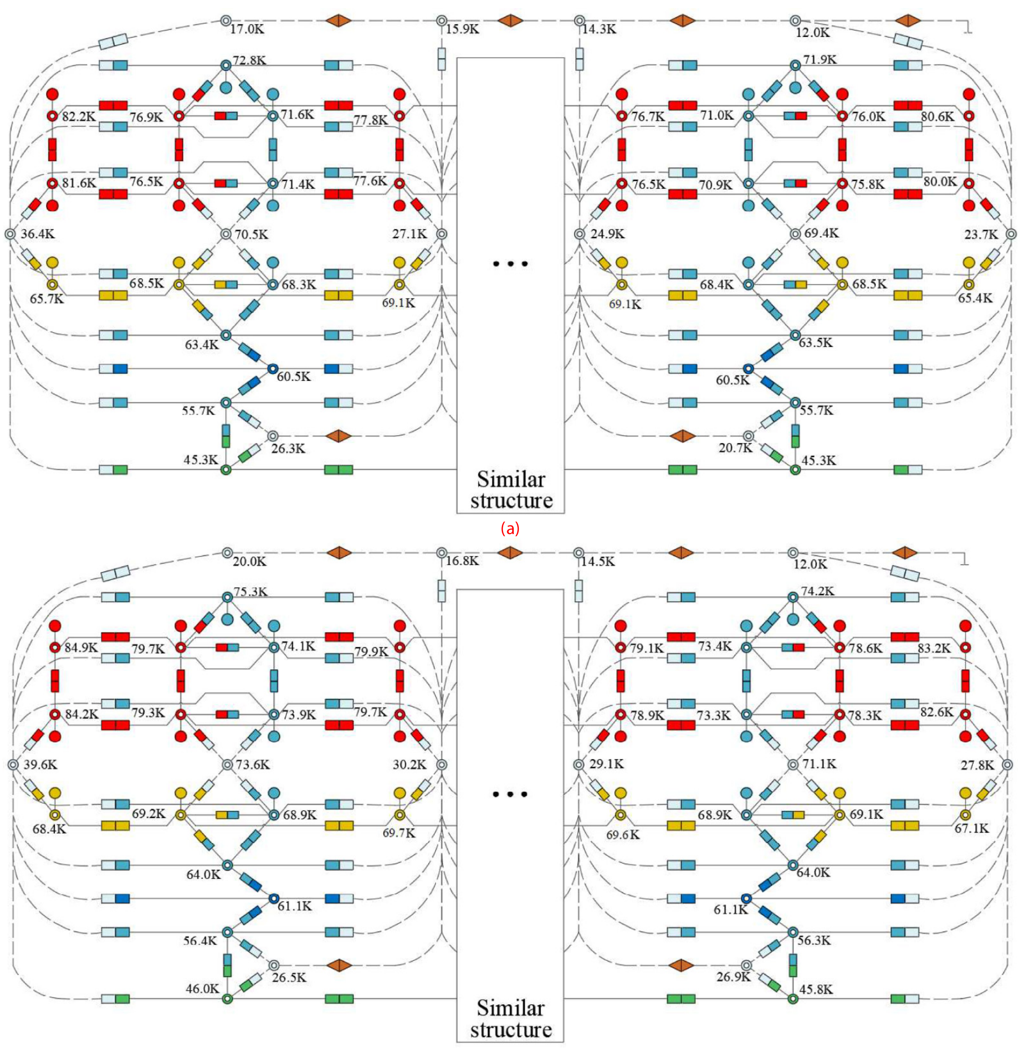

Fig. 8. Global thermal network results. (a) Unidirectional. (b) Bidirectional.

Table 5
Global temperature rise distributions of LSPMSM for bidirectional analysis (K).

Region	End	1	2	3	4	5	6	7	8	End
Stator core yoke	–	75.31	75.47	75.61	75.9	75.35	75.07	74.41	74.2	–
Stator winding	84.85	79.65	79.92	80.18	80.4	79.82	79.5	79.11	78.55	83.21
	84.19	79.27	79.69	79.99	80.18	79.71	79.17	78.94	78.43	82.57
Stator core tooth	–	74.05	74.51	74.64	74.91	74.36	73.82	73.52	73.35	–
	–	73.92	74.42	74.57	74.85	74.31	73.74	73.45	73.3	–
Rotor copper bar	–	69.21	69.71	70.08	70.31	70.21	70.01	69.62	69.14	–
Rotor core tooth	–	68.93	69.45	69.75	69.92	69.81	69.6	69.36	68.88	–
Rotor core yoke	–	64.03	64.31	64.82	64.96	64.87	64.66	64.5	63.96	–
	–	56.44	56.85	57.17	57.33	57.18	56.99	56.72	56.27	–
PM	–	61.08	61.66	61.96	62.07	61.89	61.85	61.61	61.08	–
Shaft	–	46.01	46.43	46.79	46.86	46.69	46.56	46.35	45.82	–

Table 6
Global temperature rise distributions of LSPMSM for unidirectional analysis (K).

Region	End	1	2	3	4	5	6	7	8	End
Stator core yoke	–	72.82	73.17	73.33	73.52	73.09	72.76	72.16	71.87	–
Stator winding	82.21	76.88	77.21	77.49	77.71	77.29	76.87	76.41	75.96	80.64
	81.55	76.51	76.98	77.28	77.51	77.19	76.53	76.24	75.83	80.02
Stator core tooth	–	71.57	72.21	72.29	72.55	72.11	71.61	71.15	70.98	–
	–	71.44	72.12	72.24	72.49	72.07	71.54	71.1	70.94	–
Rotor copper bar	–	68.53	69.09	69.42	69.61	69.71	69.45	69.11	68.54	–
Rotor core tooth	–	68.26	68.81	69.11	69.19	69.27	69.1	68.78	68.37	–
Rotor core yoke	–	63.35	63.65	64.21	64.32	64.3	64.13	63.97	63.47	–
	–	55.74	56.22	56.51	56.64	56.6	56.45	56.21	55.71	–
PM	–	60.45	60.99	61.32	61.45	61.39	61.25	61.04	60.5	–
Shaft	–	45.34	45.8	46.12	46.26	46.18	46.05	45.81	45.3	–

the flow rate on the drive side is less than that on the non-drive side. Therefore, the convective heat transfer coefficients of the former are smaller than those of the latter. Convective thermal resistance is inversely related to the convective heat transfer coefficient. Under the assumption of uniform heat distribution, the side with a high heat dissipation capacity has a lower temperature rise.

The axial temperature rise distribution in the stator region is shown in Fig. 9(a). In the whole stator region, the temperature rise of each structure is distributed in a W-shape along the axial direction. The lowest temperature rise in each structure is located at the stator core tooth of the non-drive side. The reasons are mainly attributed to the following two aspects. On the one hand, the end winding generates more losses than the in-slot winding. On the

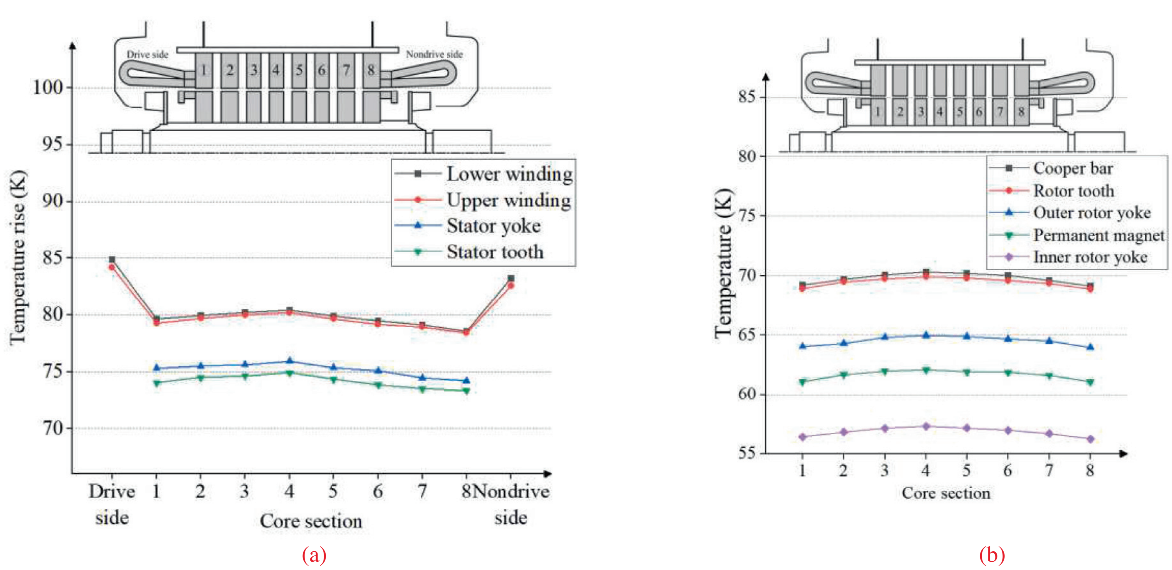

Fig. 9. Axial temperature rise distribution for bidirectional coupling analysis. (a) Stator region. (b) Rotor region.

Table 7
Specific temperature rise distribution of the stator winding.

Locations	Upper winding (K)	Lower winding (K)
The drive side end	84.2	84.9
1	79.3	79.7
2	79.7	79.9
3	80.0	80.2
4	80.2	80.4
5	79.7	79.8
6	79.2	79.5
7	78.9	79.1
8	78.4	78.6
The non-drive side end	82.6	83.2

other hand, the heat dissipation condition of the in-slot winding is better than that of the end winding due to the radial ventilation duct and stator core. The thermal resistance between the copper conductor of the in-slot winding and the stator core is less than that between the copper conductor of the end winding and the air. So, the temperature rise of the end-winding is higher than that of the in-slot winding.

The axial temperature rise distribution in the rotor region is shown in Fig. 9(b). The temperature rises in the rotor region range from 56.3 K to 70.3 K. Different from the temperature rise distribution in the stator region, the highest temperature rise in the rotor region is in the middle, which is at the copper bar of the No. 4 core section, while the lowest temperature rise is located at the end, which is at the No. 8 core section. Only minimal losses are generated in the rotor region when the motor is operating. Therefore, the temperature rise distribution in this region depends mainly on the cooling capacity. As analyzed in the previous section, the closer to the axial center, the lower the air flow and the higher the air temperature in the active region of the motor. So, the heat dissipation in the middle region is less than in the two ends, leading to a higher temperature rise.

Table 7 lists the specific temperature rise distribution of the winding. As can be seen from Table 7, the maximum temperature rise occurs in the lower winding on the drive side, and the lowest temperature rise occurs in the upper winding at the No. 8 core section. Besides, the temperature rise of the lower winding is slightly higher than that of the upper winding. It is because the cold air comes into contact with the upper winding first and exchanges heat. The air temperature increases after heat absorption. When air is in contact with the lower winding, the temperature difference between the two is smaller than that between the upper winding and air, which weakens convective heat exchange. Since the lower winding is given the same heat source as the upper winding, the temperature rise of the former is higher than the latter.

The radial temperature rise distribution at the No. 4 core section is shown in Fig. 10. It can be seen that along the radial direction from inside to outside, the motor temperature rise rises first and then falls. The highest temperature in the radial direction is located at the stator winding. Moreover, because most losses are generated in the stator region, the overall average temperature rise in the stator region is higher than that in the rotor region. In addition, the temperature gradient along the radial direction inside the stator winding and core is relatively small due to the high thermal conductivity of copper and silicon steel sheets. The heat in the rotor

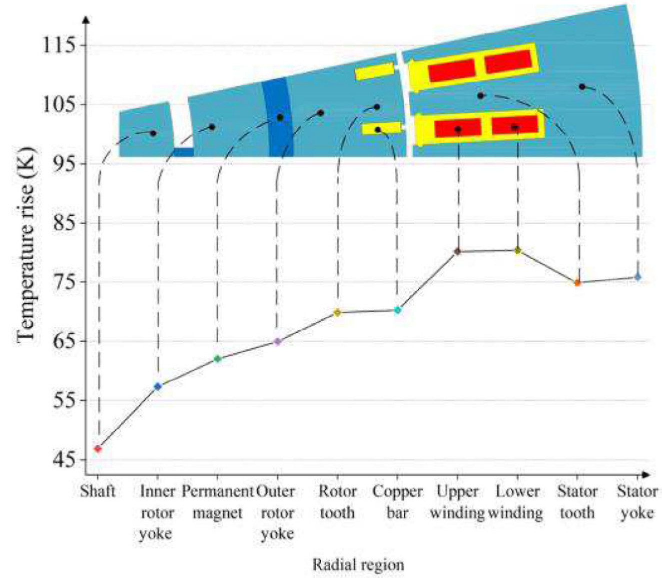

Fig. 10. Radial temperature rise distribution of LSPMSM.

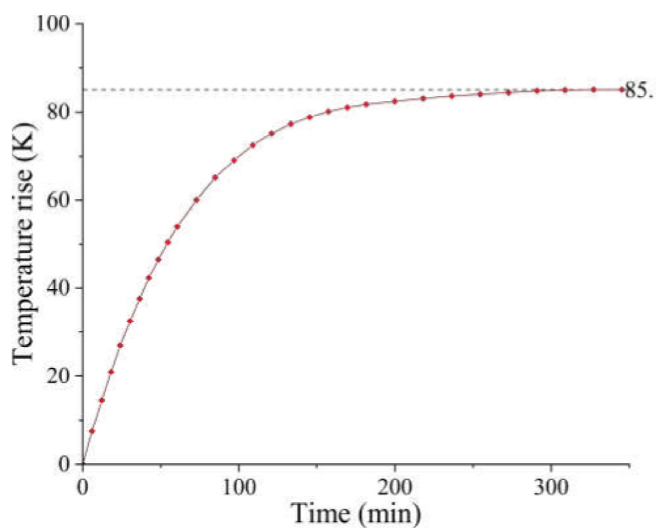

Fig. 11. Temperature rise curve with time.

region mainly comes from the stator region, so the farther away from the stator region, the lower temperature rise. And the temperature gradient inside the rotor region is relatively large.

3.3. Experimental results

Fig. 11 shows the curve of temperature rise with time during the experiment. Table 8 shows the comparison between calculated values and experimental data. The relative error between the calculated value obtained from bidirectional coupling analysis and experimental data is 2.2% and 2.9%, which meets the requirement of engineering calculation accuracy. And the relative error between

Table 8
Temperature rise comparison.

Position	Experiment	Unidirectional coupling analysis		Bidirectional coupling analysis	
	Temperature rise (K)	Temperature rise (K)	Relative error (%)	Temperature rise (K)	Relative error (%)
Lower end winding	85.1	80.6	5.3	83.2	2.2
Upper end winding		80.0	6.0	82.6	2.9

the bidirectional coupling analysis result and experimental data is smaller than that between the unidirectional coupling analysis result and experimental data, which verifies the effectiveness of the proposed method.

4. Conclusion

In this paper, the fluid-thermal characteristics of a high-voltage, 10 kV, 280 kW LSPMSM with axial and radial mixed ventilation cooling were achieved based on bidirectional hydraulic-thermal network coupling. The main conclusions were as follows:

1) Considering the structural features of the motor's axial and radial mixed ventilation cooling, the global hydraulic network model was established by modeling the indenter elements and hydraulic resistances. The motor is zoned, and the equivalent heat transfer model for each zone is established. Then the connection of local thermal network models constitutes a global thermal network model. Through the bidirectional coupling calculation of the hydraulic and thermal network model, the interaction between the air and temperature is fully considered. The relative error between the calculated and experimental results was 1.5% and 2.4%, which proves the accuracy of the calculation method.
2) The total flow of the internal air path was 0.489 m^3/s. The flow of the end region was 0.170 m^3/s, and the flow of seven radial ventilation ducts was 0.319 m^3/s. The air flow along the axial direction showed a distribution of large at both ends and small in the middle. Moreover, the flow on the non-drive side is higher than that on the drive side due to temperature differences.
3) The temperature rise of the motor approximately showed an axially symmetrical distribution. The temperature rise in the stator region is distributed in a W-shape along the axial direction. While the axial temperature distribution of the rotor area is different that of the stator region. The maximum temperature rise is 84.9 K and appears at the lower end-winding on the drive side. Moreover, the temperature rise in the drive side region is slightly higher than in the non-drive side region.

Declaration of Competing Interest

The authors declare that they have no known competing financial interests or personal relationships that could have appeared to influence the work reported in this paper.

Acknowledgments

This work was supported in part by the National Natural Science Foundation of China, under Grants (52077047), and in part by Changzhou Science and Technology Bureau, under Grants (CZ20220023).

References

[1] H. Isfahani, S. Vaez-Zadeh, Line start permanent magnet synchronous motors: Challenges and opportunities, Energy 34 (11) (2009) 1755–1763.
[2] Y. Yang, B. Bilgin, M. Kasprzak, S. Nalakath, H. Sadek, M. Preindl, J. Cotton, N. Schofield, A. Emadi, Thermal management of electric machines, IET Electr. Syst. Transp. 7 (2) (2017) 104–116.
[3] F. Zhang et al., A thermal modelling approach and experimental validation for an oil spray-cooled hairpin winding machine, IEEE Trans. Transp. Electrif. 7 (4) (2021) 2914–2926.
[4] W. Li, Z. Cao, X. Zhang, Thermal analysis of the solid rotor permanent magnet synchronous motors with air-cooled hybrid ventilation systems, IEEE Trans. Ind. Electron. 69 (2) (2022) 1146–1156.
[5] C. Sciascera, P. Giangrande, L. Papini, C. Gerada, M. Galea, Analytical thermal model for fast stator winding temperature prediction, IEEE Trans. Ind. Electron. 64 (8) (2017) 6116–6126.
[6] Q. Chen, Z. Zou, B. Cao, Lumped-parameter thermal network model and experimental research of interior pmsm for electric vehicle, CES Trans. Electr. Mach. Syst. 1 (4) (2017) 367–374.
[7] J. Qi, W. Hua, H. Zhang, Thermal analysis of modular-spoke-type permanent-magnet machines based on thermal network and FEA method, IEEE Trans. Magnet. 55 (7) (2019) 1–5.
[8] J. Lee, H. Yeo, H. Jung, T. Kim, J. Ro, Electromagnetic and thermal analysis and design of a novel-structured surface-mounted permanent magnet motor with high-power-density, IET Electr. Power Appl. 13 (4) (2019) 472–478.
[9] B. Zhang, R. Qu, J. Wang, W. Xu, X. Fan, Y. Chen, Thermal model of totally enclosed water-cooled permanent-magnet synchronous machines for electric vehicle application, IEEE Trans. Ind. Appl. 51 (4) (2015) 3020–3029.
[10] C. Kim, K. Lee, Thermal nexus model for the thermal characteristic analysis of an open-type air-cooled induction motor, Appl. Therm. Eng. 112 (2017) 1108–1116.
[11] H. Yeo, H. Park, J. Seo, J. Ro and H. Jung, Coupled electromagnetic-thermal analysis of a surface-mounted permanent-magnet motor with overhang structure, in: 2016 IEEE Conference on Electromagnetic Field Computation (CEFC), 2016, pp. 1-1.
[12] L. Mo, X. Zhu, T. Zhang, L. Quan, Y. Wang, J. Huang, Temperature rise calculation of a flux-switching permanent-magnet double-rotor machine using electromagnetic-thermal coupling analysis, IEEE Trans. Magnet. 54 (3) (2018) 1–4.
[13] T.A. Jankowski et al., Development and validation of a thermal model for electric induction motors, IEEE Trans. Ind. Electron. 57 (12) (2010) 4043–4054.
[14] T. Dong, X. Zhang, F. Zhou, B. Zhao, Correction of winding peak temperature detection in high-frequency automotive electric machines, IEEE Trans. Ind. Electron. 67 (7) (2020) 5615–5625.
[15] V. Madonna, A. Walker, P. Giangrande, G. Serra, C. Gerada, M. Galea, Improved thermal management and analysis for stator end-windings of electrical machines, IEEE Trans. Ind. Electron. 66 (7) (2019) 5057–5069.
[16] W. Tong, S. Wu, R. Tang, Totally enclosed self-circulation axial ventilation system design and thermal analysis of a 1.65-MW direct-drive PMSM, IEEE Trans. Ind. Electron. 65 (12) (2018) 9388–9398.
[17] R. Camilleri, D.A. Howey, M.D. McCulloch, Predicting the temperature and flow distribution in a direct oil-cooled electrical machine with segmented stator, IEEE Trans. Ind. Electron. 63 (1) (2016) 82–91.
[18] B.C. Guo, Y.K. Huang, Y.G. Guo, J.G. Zhu, Thermal analysis of the conical rotor motor using LPTN combined with fluid simulation, in: 2015 IEEE International Conference on Applied Superconductivity and Electromagnetic Devices (ASEMD), 2015, pp. 128–129.
[19] D.A. Howey, P.R.N. Childs, A.S. Holmes, Air-gap convection in rotating electrical machines, IEEE Trans. Ind. Electron. 59 (3) (2012) 1367–1375.
[20] A. Mohamed, A. Hemeida, A. Rasekh, H. Vansompel, A. Arkkio, P. Sergeant, A 3D dynamic lumped parameter thermal network of air-cooled YASA axial flux permanent magnet synchronous machine, Energies 11 (4) (2018) 774.
[21] A. Rasekh, P. Sergeant, J. Vierendeels, Convective heat transfer prediction in disk-type electrical machines, Appl. Therm. Eng. 91 (2015) 778–790.
[22] Y. Gai et al., Numerical and experimental calculation of CHTC in an oil-based shaft cooling system for a high-speed high-power PMSM, IEEE Trans. Ind. Electron. 67 (6) (2020) 4371–4380.
[23] D.A. Staton, A. Cavagnino, Convection heat transfer and flow calculations suitable for electric machines thermal models, IEEE Trans. Ind. Electron. 55 (10) (2008) 3509–3516.
[24] J. Li, Y. Lu, Y.-H. Cho, R. Qu, Design, analysis, and prototyping of a water-cooled axial-flux permanent-magnet machine for large-power direct-driven applications, IEEE Trans. Ind. Appl. 55 (4) (2019) 3555–3565.
[25] N. Simpson, R. Wrobel, P. H. Mellor, Estimation of equivalent thermal parameters of impregnated electrical windings, IEEE Trans. Ind. Appl., 49(6) (2013) 2505-2515.